Effect of the process gas and scan speed on the properties and productivity of thin 316L structures produced by Laser-Powder Bed Fusion

Effect of the Process Gas and Scan Speed on the Properties and Productivity of Thin 316L Structures Produced by Laser-Powder Bed Fusion

C. PAUZON, A. LEICHT, U. KLEMENT, P. FORÊT, and E. HRYHA

The development of the laser powder bed fusion (L-PBF) process to increase its robustness and productivity is challenged by ambitious design optimizations, such as thin wall structures. In this study, in addition to the effect of commonly used gases as Ar and N_2, increased laser scanning speed and new process gases, such as helium, were successfully implemented. This implementation allowed to build 316L stainless steel components with thin walls of 1 mm thickness with an enhanced build rate of 37 pct. The sample size effect and the surface roughness were held responsible for the reduction in strength (YS > 430 MPa) and elongation (E_{AB} > 30 pct) for the 1 mm samples studied. Similar strength was achieved for all process gases. The increased scanning speed was accompanied by a more random texture, smaller cell size, and grain size factor along the building direction when compared to the material built with the standard laser parameters. Stronger preferential orientation ⟨101⟩ along the building direction was observed for material built with standard parameters. Finally, the use of helium as a process gas was successful and resulted in reduced cell size. This finding is promising for the future development of high strength 316L stainless steel built with high build rates.

https://doi.org/10.1007/s11661-020-05923-w

I. INTRODUCTION

LASER-POWDER bed fusion (L-PBF) uses the energy from a laser to locally melt and solidify a bed of metallic powder. Subsequently applying layers of powder and exposing them to radiation in a controlled manner allows one to build 3D parts of relatively high complexity and resolution at rather low cost. This ability explains L-PBF's broad adoption by various industries, such as aerospace, automotive, and medicine. While the demand for new materials is constantly increasing to satisfy a broad range of applications, some materials offering good processability and high mechanical performances are well-established as 316L stainless steel.

The main role of the gas is to control the oxidation of the material during the process and remove the by-products generated during the process. Usually flowing from one side to another over the build plate, covering the process area, the gas applies a drag force on particles crossing its path. As a result, it tends to entrain the by-products into its streamlines toward the outlet and thus away from the melt pool and potential interaction with the laser beam. Bin *et al.*[1] modelled the argon flow and its effect on the trajectories of by-products of different sizes, highlighting the importance of its optimization to limit harmful redepositions.

The standard gas used to establish a protective atmosphere for the L-PBF process is argon and sometimes nitrogen for materials that are not too sensitive to nitrogen pick-up, mainly steels (*e.g.*, 316L stainless steel, maraging steel). Argon is a noble gas, and nitrogen is relatively inert. By flushing these species into the process chamber, impurities such as oxygen can be diluted and reduced to 1000, 100, or even 10 of ppm. As the powder bed is exposed to the laser radiation, its temperature rises tremendously in a short time.[2] This heat increase is likely to trigger diffusion-controlled reactions, such as oxidation or nitridation, through the interaction of the material with the surrounding atmosphere.[3] In addition to affecting the chemistry of the produced parts, the degradation and recyclability of the powder particles can be compromised.[4] Our previous work[5] demonstrated that atmosphere purity of 1000 ppm O_2 and below allows high mechanical performances for 316L stainless steel, exceeding the one for wrought material. It was also highlighted that the atmosphere purity can be critical for the surface oxidation state of 316L powder upon oxygen levels of 2000 ppm and above. The results

C. PAUZON, A. LEICHT, U. KLEMENT, and E. HRYHA are with the Chalmers University of Technology, Department of Industrial and Material Science, S41296 Göteborg, Sweden. Contact e-mail: pauzon@chalmers.se P. FORÊT is with the Linde AG AT EMEA, Carl-von-Linde-Stra&\rbetae 25, 85716 Unterschlei&\rbetaheim, Germany.

Manuscript submitted February 3, 2020.

Published online: 04 August 2020

also suggest that processing under nitrogen in comparison to argon does not significantly affect the obtained microstructure nor the mechanical properties.

The present work focuses on more critical design features: thin walls. L-PBF allows for the production of complex geometries at reduced cost compared to traditional machining operations. Considerable effort is invested in the development of thin walls and lattice structures, which enables one to achieve lightweight or increased specific surface area of the parts.[6–11] These features are essential for many applications, such as heat exchangers in the energy and gas sectors. A recent study conducted by Abele *et al.*[12] focused on laser parameter optimization to achieve controlled porosity and permeability for applications, such as fuel cells, which require defined mass transport through thin wall structures. Because of their high aspect ratio, their thermal history and the resulting microstructure and mechanical properties differ significantly from that of bulk parts. Indeed, the solidification of the exposed powder bed is influenced by the heat input. As highlighted by the work of Rubenchik *et al.*,[13] the absorptivity of 316L stainless steel powder is about 60 pct; thus, a large fraction of the energy is being reflected. The absorbed energy is then transferred through radiation from the top surface, convection to the atmosphere, conduction to the powder bed, the solidified material, and the baseplate. Because of the solid material's higher thermal conductivity, most of the heat is transferred to the already solidified metal and further to the baseplate. For high aspect ratio geometries like thin walls, as the build height, and hence the melt pool distance to the baseplate increases, the fraction of the heat transferred to the atmosphere and the powder bed increases. Recent works by Leicht *et al.*[14] and Wang *et al.*[15] on 316L stainless steel thin walls and struts indicated significant differences in the microstructure between the bulk material and thin wall structures. It was shown that thin wall structures exhibit a more random texture and smaller grain size than bulkier specimens, which are characterized by a significant ⟨101⟩ orientation parallel to the building direction.

Therefore, it is of interest to investigate the process gas effect on the properties of thin 316L walls. The high specific area of the thin walls could promote the dissolution of nitrogen from the process atmosphere, while the use of helium could promote heat removal from the solidified material. Indeed, helium has a thermal conductivity and heat capacity an order of magnitude above that of argon and nitrogen. These outstanding thermal properties, together with its high ionization potential, explain the implementation of helium in several industrial processes connected with laser technologies, such as TIG welding of titanium.[16] The use of helium for L-PBF has been investigated by few research groups,[17,18] but the results were not promising (low as-built density), which could be connected to the stage of development of the L-PBF gas management system at the time of the investigation. Zhang attempted to implement helium as a process gas for 316L stainless steel on a Realizer SLM 250 (ReaLizer GmbH)[17] and achieved parts with densities higher than 80 pct. Similarly, Wang *et al.*[18] studied Al-12Si parts produced with a Realizer SLM 100 under argon, nitrogen, and helium. They reported relatively low and unchanged densities (about 97 pct) under these gases and noted that the material produced under helium was characterized by few isolated areas with a higher number of spherical pores. The authors did not comment on the origin of these defects. One should underline that in both mentioned early works about helium, the atmosphere was established by purging the process chamber and then maintaining a slight overpressure during the build job. No data were presented on either the achieved process atmosphere purity or the gas speed over the build plate. While argon and nitrogen have relatively similar densities, helium is about 10 times lighter, and therefore, the gas flow should be adjusted to achieve a similar gas speed. A lower gas speed results in poor shielding of the melt pool and, potentially, an accumulation of process by-products, which are likely to interact with the laser radiation and redeposit on the powder bed. Our recent research on utilization of He for L-PBF processing of Ti-6Al-4V proved high potential of this processing gas for improvement of the L-PBF process productivity (> 40 pct) without compromising mechanical properties of the material.[19,20] However, it is necessary to better understand the effect of the process gas to ensure the robustness and then the productivity of the process, which might be threatened by ambitious design features such as thin walls. This understanding will allow the greater adoption of this technology among several industrial segments. As highlighted by Babu *et al.*,[21] additive manufacturing processes need to be further developed to upscale them, ensuring high productivity. This will be a determinant for materials of relatively low cost, such as 316L stainless steel, and can be expected to garner greater research attention as hardware develops fast and integrates *in-situ* monitoring systems and more powerful energy sources. In that regard, thin walls are not only interesting for lightweight but also for process time optimization since these structures can be built faster. Therefore, determining whether strategies such as tailored gases for improved process stability and thin walls can be combined to increase build rate is of interest.

In the present study, the gas used to establish the protective atmosphere was not limited to its blanketing action but was considered as a unique process parameter. In that regard, both the standard argon and nitrogen gas were considered. The use of the noble helium gas offering high thermal conductivity and heat capacity was also studied. The microstructure and mechanical properties of thin 316L stainless steel structures built under these different process gases were investigated, and the effect of increased laser scanning speed was determined.

II. MATERIALS AND METHODS

Gas atomized 316L stainless steel powder with particle sizes between 20 to 53 μm manufactured by gas atomization was used as a feedstock material. The L-PBF machine employed to produce the samples was

an EOS M290 from EOS GmbH (Germany) equipped with a Yb-fiber laser of maximum nominal power of 400 W, a baseplate of 250 × 250 mm^2 area, and a nitrogen generator. Three process gases were considered: argon, nitrogen, and helium. High purity technical argon and helium were employed. Argon 5.0 and Helium 4.6 feature less than 10 and 40 ppm impurities, respectively. In light of previously published evidence of the limited effect of residual oxygen on 316L stainless steel properties built by L-PBF,[5] the internal generator was used to produce a nitrogen rich atmosphere (about 2000 ppm residual O_2) by filtering compressed air. Although the considered gases have different densities and thermal properties, the differential pressure of the machine was adjusted to achieve the same gas speed over the powder bed of about 2.2 m/s.

The mechanical performances of vertical near-net-shaped flat tensile specimens with a gauge thickness of 1 and 3 mm were studied. Standard specimens with geometry according to ASTM E8/E8M-15a produced with standard parameters developed by EOS GmbH for 316L stainless steel using a layer thickness of 20 μm (version 1.10) were used as a reference.[22] Additional specimens were built by increasing the scanning speed, and therefore the build rate by 37 pct and keeping the other parameters to their standard values (with respect to parameters of version 1.10). The standard process parameters are an optimized combination of laser parameters and scanning strategy. A stripe pattern strategy was applied and rotated by 67 deg between each deposited layer. No contour scanning was applied and the samples had no subsurface porosity regardless of the process atmosphere. Figure 1 illustrates the geometry of the thin sample and the used support structures (in light grey) on the sides of the gauge length. The latter were added to connect the part to the baseplate and improve the heat transfer, ensuring a successful build. Indeed, these high aspect ratio parts are likely to be subjected to curling and deformation upon collision with the recoater. Once the builds were completed, the samples were cut off the baseplate and their supports were carefully removed using a hand saw to make sure that the thin gauges were not deformed or strained. The as-built tensile samples were tested at room temperature with an Instron 5500R machine and a cross head velocity of 0.025 pct/s. The reported tensile properties correspond to average values on three specimens, and a standard deviation indicates the spread. The samples were net-shape and with a thin gauge cross-section. Hence, the measurement of the load-bearing thickness of the samples using a caliper is likely to be overestimated because of the as-built surface roughness of the L-PBF produced samples. To overcome this issue, the samples were mounted, prepared, and examined using a light optical microscope (LOM). The load-bearing thickness was measured and compared to the value obtained using the caliper. The surface roughness appeared to lead to an overestimation when measuring with the caliper of about 150 μm for all samples, regardless of the process gas, using the standard laser parameters. Samples built at higher build speed were characterized by a slightly rougher surface, leading to an overestimation of the load-bearing thickness by about 230 μm when using the caliper. Hence, the cross-section areas used for the 1 and 3 mm standard samples are 2.38 mm^2 (derived from the LOM measurements: 0.96 × 2.48 mm) and 7.01 mm^2 (i.e., 2.91 × 2.41 mm) for standard parameters and 2.26 mm^2 (*i.e.*, 0.93 × 2.43 mm) for the 1 mm samples built faster. The elongation at break (E_{AB}) of the specimens was calculated according to the ASTM E8/E8M-15a procedure by measuring the gauge length before and after testing with the caliper. The fracture surfaces of the tensile specimens were investigated with a field-emission scanning electron microscope (SEM - Leo Gemini 1550 SEM), equipped with an energy dispersive X-ray spectrometer (EDX) INCA X-sight for composition determination purposes.

One untested sample for each thickness produced in argon, nitrogen, and helium was used for further microstructural investigations. Sections of the gauge length were mounted in resin to observe the microstructure along the building direction. The samples were prepared following Struers recommendations for stainless steels. The polished samples were used to measure the relative porosity using a light optical microscope (LOM) ZEISS Axioscope 7. The measurement uncertainty is given as the standard deviation calculated for at least three measurements per sample. The cross-sections were then electro-chemically etched in a 10 pct oxalic acid solution. The revealed microstructures were studied with the LOM and SEM. Electron backscattered diffraction (EBSD) technique, using a Nordlys II detector (Oxford Instruments) and the HKL Channel 5 data processing software, was used to determine grain boundaries, grain orientations, and overall texture. An acceleration voltage of 20 kV was employed with a 1.5 μm step size. Minor noise reduction was performed on the acquired orientation maps i.e. wild spikes were removed and minor noise reduction was conducted (seven nearest neighbors required). High angle grain

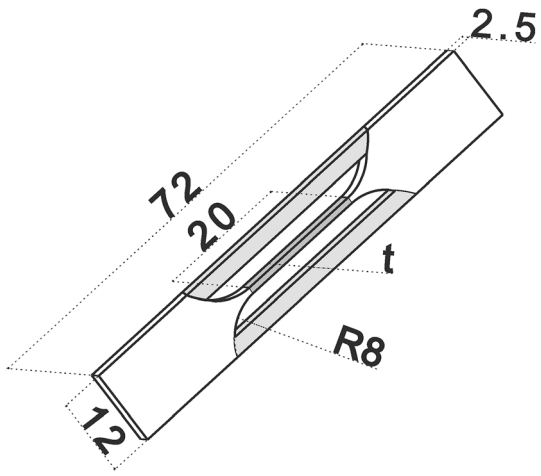

Fig. 1—Sketch of the tensile test specimen geometry with the thickness t, which was either 1 or 3 mm. The support structures are light grey; they are provided to ensure proper heat transport to the baseplate.

boundaries were defined by a misorientation larger than 10 deg and are illustrated by black lines.

In addition, the Vickers hardness HV1 (1 kg load) was measured using a DuraScan system (Struers) on the specimens and on a cube of 1 cm^3 built in argon with standard parameters. The displayed results correspond to the average of 5 to 10 measurements spaced by at least three indentation dimensions. Moreover, the oxygen and nitrogen content of the specimens built with standard parameters was assessed by carrier hot gas extraction (CGHE) with a LECO ONH836 system. For this purpose, at least three samples were extracted from the bulk of the samples within their gauge length.

III. RESULTS AND DISCUSSION

A. *Influence of Process Gas and Sample Thickness on the Chemistry, Porosity and Hardness*

Table I lists the oxygen and nitrogen contents of the samples built in the different atmospheres. While all the nitrogen initially present in the feedstock powder seems to be transferred to the built material, significant oxygen loss of up to about 200 ppm was registered. A similar result was already reported[5] and attributed to the removal of the surface bound oxygen, present on powder feedstock due to the high surface area, and oxygen removal by transfer to projections. Regardless of the process atmosphere, the 1 mm samples picked up more oxygen than the 3 mm samples, see Table I. This is likely connected to the higher specific surface area of the thin specimens and the corresponding heat accumulation during L-PBF processing.

The lowest oxygen (and nitrogen) contents are reported for the samples produced under argon. The highest oxygen contents obtained with nitrogen gas can be attributed to the higher residual oxygen partial pressure in the processing atmosphere produced by the internal nitrogen generator. As previously shown, this system allows to achieve oxygen levels of about 2000 ppm O_2 compared to technical gas, which usually results in less than 800 ppm O_2.[5] The slightly higher oxygen contents measured for the helium specimens could be related to the non-optimal oxygen calibration and sensors of the L-PBF machine for helium. Soon after starting the process, the sensor displayed 0 pct O_2. It is important to highlight that the calibration of the oxygen sensors is conducted by setting them to 21 pct O_2 when measuring in the laboratory atmosphere of much higher density than helium. Electrochemical oxygen sensors are known to be sensitive to the carrier gas molecular weight since it affects the rate at which oxygen molecules can reach the sensor's cell. In addition, this 21 pct O_2 calibration is quite far from the expected oxygen processing range (< 0.1 pct O_2). Finally, the low density of helium can lead to misreading. For example, the light helium could accumulate at the top of the process chamber—above the O_2 molecules—where the sensors are placed, and these could underestimate the actual oxygen level. Still, a constant "holding" flow of several L/min ensures a relatively low impurity level, as reflected by the oxygen and nitrogen content in the helium samples (see Table I). This holding flow is initially present to counteract possible leaks when the gas recirculation within the process chamber starts.

Overall, this appears to be acceptable for the robust grade 316L stainless steel, and the reported oxygen and nitrogen differences can be considered small. In comparison to recently published work,[23] the measured oxygen seems to be higher and this result is connected to the higher oxygen content from the feedstock powder used herein. Both work highlight a significant oxygen loss from the powder to the built material. For more sensitive materials, such as Al and Ti alloys, an adapted oxygen monitoring system is likely necessary,[24] in particular for the implementation of lighter process gases. Besides, nitrogen levels are slightly higher in the helium and nitrogen specimens than in the argon specimens. As mentioned, the process atmosphere is established by flushing the process chamber, so impurities like oxygen and nitrogen initially present in the laboratory air (about 21 pct oxygen and 78 pct nitrogen) are diluted. This explains the higher nitrogen pick-up accompanying the higher oxygen pick-up of the nitrogen and helium samples. Similar conclusions can be drawn for the samples produced using a higher scanning speed.

The LOM observations of the polished specimens revealed a high relative density of at least 99.97 ± 0.01 pct using the standard laser parameters for all the process atmospheres, regardless of the samples' thickness. This result is similar to those obtained for standard bulk 316L stainless steel specimens produced under argon and nitrogen.[5] Unlike the laser power and the scanning speed, as shown by Sander *et al.*,[25] or the exposure time as reported by Cherry

Table I. Contents of O and N of the Powder Feedstock and the Produced Specimens with Standard Parameters in Argon, Helium, and Nitrogen from the Generator, for the 1 mm and 3 mm Thick Specimens

Process Gas	Sample Thickness	Oxygen (ppm)	Nitrogen (ppm)
Feedstock Powder	—	786	1240
Argon	1 mm	584	1300
	3 mm	555	1300
Helium	1 mm	621	1330
	3 mm	585	1320
Nitrogen Generator	1 mm	643	1360
	3 mm	585	1360

et al.,[26] the change of process atmosphere does not compromise the density of the built parts in the current study when standard process parameters for 316L in the EOS M290 are used. The build rate increase of 37 pct using a higher scanning speed predictably came along with a slight density reduction. Among all the specimens quickly built, the relative density was still at least 99.93 ± 0.01 pct.

Table II displays the Vickers hardness for the produced specimens as well as the respective values for a standard cube produced in argon. The nitrogen- and helium-produced specimens seem slightly harder, which could be related to the potential difference in microstructure (as shown below) and the higher nitrogen pick-up for these samples (see Table I), which is known for its solution strengthening effect of austenite.[27] Still, considering standard deviation, similar microhardness was obtained. The properties obtained are homogeneous, as suggested by the tensile test results depicted below.

B. *Influence of the Process Gas and Wall Thickness on the Microstructure*

Figure 2 shows the microstructure along the building direction within the gauge of the 1 mm thick tensile specimens produced under helium with standard parameters. Similar observations were made on the samples built in argon and nitrogen, as well as on the 3 mm specimens and standard geometry tensile bars, regardless of the laser scanning speed (even though the samples produced faster consisted of more lack-of-fusion defects).

Table II. Vickers Hardness HV1 of the Produced Specimens with Standard Parameters in Argon, Helium, and Nitrogen from the Generator and a Cube (1 cm^3) Produced Under Standard Argon

Process Gas	Sample Thickness	HV1
Argon	Cube 10 × 10 × 10 mm^3	244 ± 6
Argon	1 mm	239 ± 10
	3 mm	242 ± 8
Helium	1 mm	239 ± 13
	3 mm	253 ± 7
Nitrogen Generator	1 mm	248 ± 7
	3 mm	251 ± 9

The typical features of 316L stainless steel built by L-PBF can be distinguished. The hierarchical microstructure consisting of rounded melt pool boundaries is characterized by dark contrast and submicron-sized cellular structure of light contrast. The boundaries of the submicron-sized cells (see Figure 2(b)) were identified as rich in Cr and Mo and act as a dislocation pinning network responsible for the steady hardening of the produced material.[28,29] These are selectively etched by the oxalic acid solution. The distance between melt pool boundaries along the building direction varies significantly across the gauge section up to 50 to 60 μm, as reported elsewhere.[14] This suggests that L-PBF of 316L stainless steel is self-healing since the energy input allows re-melt of several deposited layers and eventually repair defects, such as lack-of-fusion porosity. By employing a wider process parameters window covering high and low energy inputs, one could better observe the different effect of the gases on porosity and microstructure. Furthermore, the process parameters of prime importance, such as the laser power, the scanning speed, and the hatch distance have a limited impact on the observed microstructures. The work of Leicht *et al.*[30] highlights that upon varying these parameters, and thus the volumetric energy density input to about half its recommended standard value, the relative density is lowered by only 1 pct. While the authors also identified significant changes in the grain structure by EBSD, these changes could not be established only by SEM observations like those presented in Figure 2. Besides, the self-healing property of the process, the good processability of 316L stainless steel can also be attributed to the single phase austenitic structure over the solidification range and high ductility and hence limited risks of cracking upon rapid solidification and cooling.

Although no significant microstructural differences were seen between the samples of different thicknesses produced using different gases and scanning speed at the magnifications investigated in Figures 2(a) and (b), the size of the cells, distinguishable in Figure 2(b), is highly

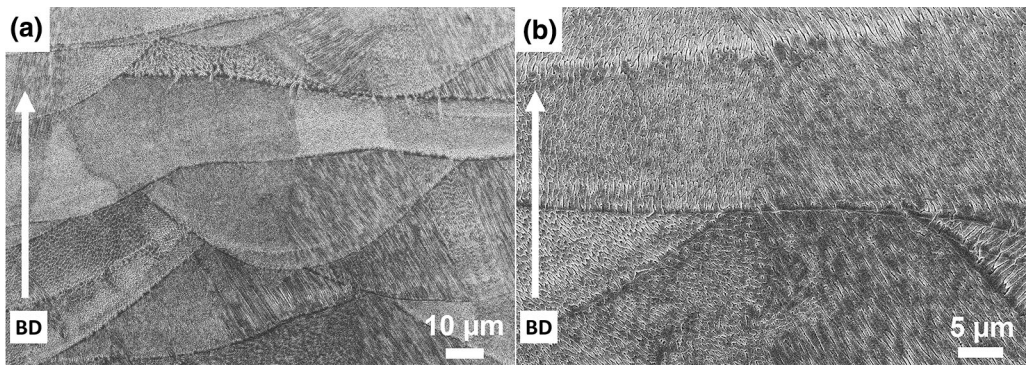

Fig. 2—SEM micrographs along the building direction (BD indicated by the white arrow) within the gauge length of the 1 mm tensile specimens produced under helium with standard laser parameters for low (*a*) and high (*b*) magnifications.

dependent on the thermal history.[22,31] The cell size was measured for the produced specimens using high magnification micrographs of areas of equiaxed cell appearance. More than 10 micrographs similar to the ones presented in Figures 3(a) and (b) were collected across the gauge length and analyzed to gather statistically relevant data, as described elsewhere.[31] In general, the cellular structure observed across the gauge cross-section varies significantly (see Table III) and in a relatively random manner, which highlights the important variations in local cooling gradients' magnitudes and directions (see Figure 3). Still, the following conclusions can be drawn. The average cell size decreases by about 100 nm for the 1 mm thick sample compared to the 3 mm sample under argon and helium. The samples produced under helium seem to exhibit a finer average cell structure of about 550 nm (for the 1 mm thickness) compared to argon (about 650 nm) and nitrogen (about 800 nm). The fine cellular structure produced with helium could be caused by a locally higher cooling rate of the dynamic melt pool owing to the higher thermal conductivity of helium. Besides being a high thermal conductivity noble gas, helium's low kinematic density allows to avoid the accumulation of the hot vapors and projections generated above the gas-liquid metal interface. The larger average cell size for nitrogen specimens could be due to the state of the surface of the powder particles exposed to the nitrogen atmosphere generated by the internal generator. As shown by Pauzon *et al.*,[5] these particles are covered with Cr-Mn-Si rich oxides. These oxides' formation is likely to be promoted by the higher oxygen potential at the particle surface. This, in turn, tends to promote lack-of-fusion defects and only partial melting of the particles, resulting in residues of the initial powder microstructure present in the built material, as can be observed in Figure 3(c).

Leicht *et al.*[30] demonstrated, and this work confirms, that even though 316L stainless steel is a robust material of low susceptibility to performance variations, it is still subjected to microstructural changes when tuning process parameters, such as cell size and preferential grain orientation. EBSD orientation maps of the 1 mm thick samples produced in each gas with standard parameters are provided in Figure 4. As the maps of the 3 mm specimens produced with standard parameters are similar to those presented, these are not displayed. The presented results are representative and selected from several maps taken at different locations on different cross-sections. The orientation maps are provided in the building direction with the corresponding inverse pole figures. All produced samples reveal a complex grain structure that contains large elongated grains in combination with small and almost equiaxed grains. The constant movement of the heat source (*i.e.*, the laser beam) makes the grains twisted and curved since the angle of the temperature gradient is repetitively changed. The direction of the temperature gradient will, however, always be directed upward (following the building direction), creating elongated grains that grow epitaxially through several melt pools.

The ⟨001⟩ orientation is the easy-growth direction for most fcc metals including 316L stainless steel.[32–35] Still, 316L stainless steel produced by L-PBF can exhibit both a random texture and a stronger ⟨001⟩ or ⟨101⟩ texture.[31,35] The texture is affected by both the process parameters and the scan strategy.[36,37] As Figure 4 depicts, the microstructure of the produced samples for all three gases appears to have a ⟨101⟩ preferential orientation in the building direction. Hence, the EBSD analysis revealed no significant differences between the two thicknesses nor between the different gases for standard laser speed. Because the heat capacity and thermal conductivity of helium is one order of magnitude higher than that of argon and nitrogen, helium could potentially extract heat more efficiently than the other gases from the melted areas by conduction at the gas–component and gas–powder bed interfaces. The change in gas type does not seem to significantly affect either the intensity or the direction of the heat flow aligned along the building direction. As a consequence, the pronounced ⟨101⟩ texture is still observed. However, as mentioned, efficient removal of the heat from the process gas–component interface will not change the direction of the heat flow, only its magnitude, and therefore minimum effect on the texture is expected, as observed here. However, the thermal properties of the gas could have a greater impact on the microstructure for a material with lower thermal conductivity than

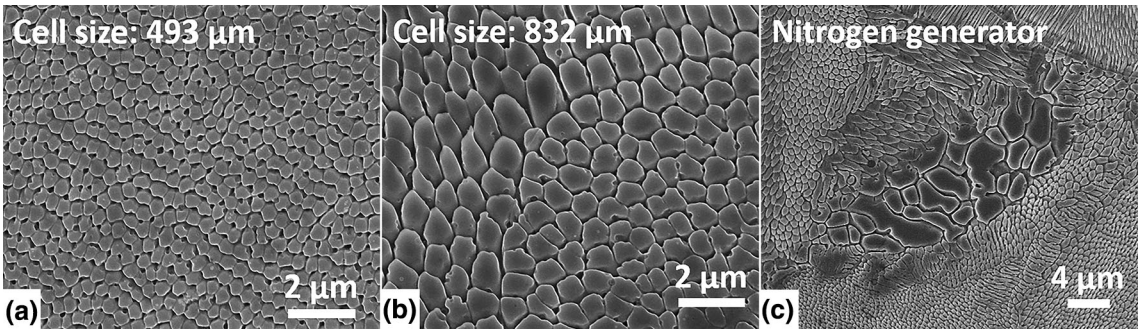

Fig. 3—(*a*), (*b*) High magnification SEM micrographs depicting the cellular structure of the 316L stainless steel specimens (1 mm thick) built by L-PBF produced using helium of high purity. The two images highlight the important variations of cell size within one sample, thus stressing the difficulty of an accurate and conclusive interpretation. (*c*) The micrograph identifies the retained microstructure from a not-fully-melted powder particle under nitrogen processing with the internal generator.

Table III. The Cell Size Measurements for the 1 and 3 mm Thick Samples Built Under the Different Atmospheres With the Two Laser Scanning Speeds

Process Gas	3 mm and Standard Speed (nm)	1 mm and Standard Speed (nm)	1 mm and Higher Speed (nm)
Argon	756 ± 223	648 ± 357	718 ± 422
Nitrogen	825 ± 660	821 ± 545	550 ± 323
Helium	655 ± 438	553 ± 351	530 ± 275

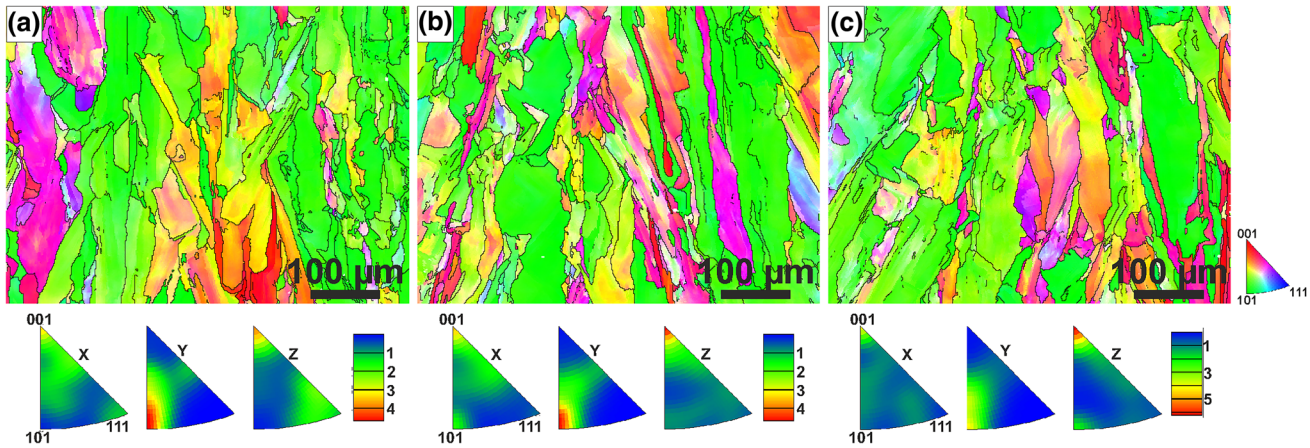

Fig. 4—EBSD orientation maps (in building direction) of the center of the 1 mm tensile specimens produced in (*a*) argon, (*b*) nitrogen, and (*c*) helium.

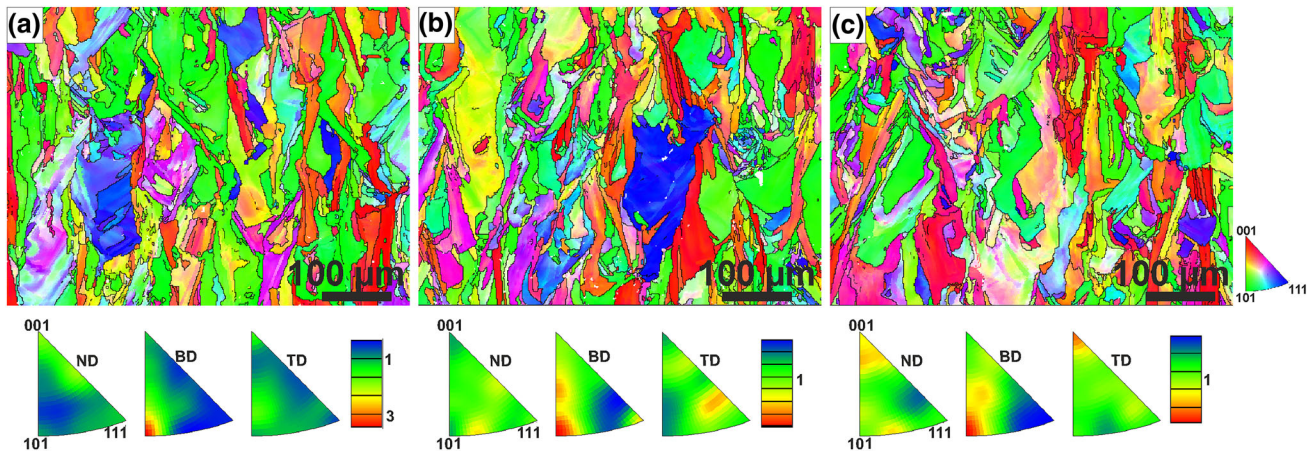

Fig. 5—EBSD orientation maps (in building direction) of the 1 mm tensile specimens produced with higher laser scanning speed (extra 37 pct) in (*a*) argon, (*b*) nitrogen, and (*c*) helium.

316L stainless steel (13.75 W/m K calculated using JMatPro), for example Ti-6Al-4V (6.7 W/m K).

EBSD orientation maps of the 1 mm thick samples produced in each gas with increased scanning speed are provided in Figure 5. First, no notable differences are observed between the investigated gases. Still, all three maps reveal a much weaker texture than that of the samples produced with the standard laser scanning speed. The weaker texture is associated with the reduced energy density input into the part, as shown by Leicht *et al.*[30] Furthermore, the grains appear smaller than the grains obtained using the standard scanning speed. Grain size of the L-PBF-produced 316L stainless steel part is difficult or even impossible to measure accurately due to the grains' complex 3D morphology. Still, the grain size difference along the building direction of the 1 mm samples built with standard (Figure 4) *vs* increased scanning speed (Figure 5) is striking. In an attempt to quantify this difference, one can apply the mean intercept length method to compute the grain size factor on the cross-section showing the grains along the building direction. This cross-section was preferred as it highlights possible differences in grain dimensions mostly along the building direction resulting from their epitaxial growth. This size factor is obviously not a direct measurement of grain size since it does not

account for the grain shape (and will vary considerably when computing it on a cross-section parallel to the baseplate). The factor was calculated by drawing randomly oriented lines and marking all the intersections of these lines with grains. The grain size factor can then be derived as the total line length divided by the number of intercepts. The average grain size factor measured for the investigated samples are listed in Table IV. It appears that the grain size factor along the building direction for the samples built with standard scanning speed remains unchanged. However, when using the increased scanning speed, the size factor is notably reduced (by at least 30 pct). Therefore, the increased build rate restricted grain growth and, therefore, the associated texture. In comparison, the process gas seems to have a greater influence on the local heat flow at the scale of the solidification of a single melt pool and the formation of the cellular structure rather than on the global vertical heat flow at the scale of the full component.

C. *Influence of the Process Gas and Wall Thickness on Tensile Properties and Fracture Behavior*

The samples with dimensions in accordance to the ASTM E8/E8M-15a standards exhibit high mechanical performances (YS = 539 ± 7 MPa) and elongation at break (61 ± 4 pct).[22] As mentioned, the dislocations accumulate at the cells. At low strains, these cells remain mostly unchanged in shape and size,[29] hindering the movement of dislocation for a longer period, which is reflected in the steadier work hardening and the improved ductility.[29,38,39] Upon higher strain, cells are deformed, and deformation by twinning is favored; both enhance elongation.[29,40]

Figure 6 displays the tensile properties of the specimens produced under the different atmospheres. At first glance, the 1 mm samples exhibit overall lower strength and elongation, accompanied with more scatter in elongation than the 3 mm samples, see Figure 7(a). It is also evident that the 1 mm samples have mechanical performances notably below that of the standard specimens, while the 3 mm samples are approaching those. This lower performances of the thinner specimens may be explained by a phenomenon known as the size effect.[41] A common analogy illustrates the size effect as follow. The sample loaded in tension is similar to a chain. Sections of the gauge length consisting of several grains are links of this chain. As observed in the EBSD analysis section, the grain size and texture remained mostly unchanged between the 1 and 3 mm thick specimens built using standard process parameters. The yielding of the chain will be initiated at the weakest link. Since surface roughness does not affect the yield strength (YS), the weakest link will be the section for which the grains have the least favorable orientation to deform upon loading. This could be determined by calculating the critical resolved shear stress to find out which slip systems are preferentially activated. Without engaging in such calculations, one can follow this reasoning: The links of the 3 mm sample chain will contain more grains than that of the 1 mm, and therefore, the distribution of the different oriented grains among the links will be more uniform. In other words, the probability that a link of the 1 mm sample chain is weak is higher because it is composed of fewer grains.

Figure 8 shows micrographs of the fracture surfaces for the 1 mm (argon and nitrogen) and 3 mm (argon) samples. The fracture of the thin specimens features the presence of a significant number of crack initiation points at or close to the surface that further propagate through the sample cross-section. This is reflected by the presence of large defects, mainly cracks, as seen in Figures 8(a) and (b), and lack-of-fusion defects as seen in Figures 8(c) and (d). The thicker specimens offered more load bearing material so that the center of the fracture surface clearly highlights a ductile failure with some micro-cracks, micron-sized dimples, and evenly distributed spherical oxides, see Figures 8(e) and (f). This is the typical fracture behavior for 316L stainless steel built by L-PBF, as reported elsewhere.[5,31,42,43] The dramatic influence of surface and near-surface defects for the thin specimens is likely to also have contributed to the early necking and the spread in elongation at break. The common appearance of the fracture surface is consistent with the good repeatability of material performances in the different atmospheres.

The previous EBSD results highlighted that the samples built with the higher laser scanning speed are characterized by a notably smaller grain size factor along the building direction and a more random crystallographic structure than the samples built with the standard scanning speed. Furthermore, the quickly built samples were characterized by finer cells. Although the measurement accuracy can be discussed, increasing the scanning speed leads to smaller cell size.[22] Therefore, these specimens are expected to be stronger than standard ones following the Hall–Petch relation. As emphasized by Yuan *et al.*,[44] YS and flow stress are a result of the displacement of dislocations following given slip systems. These dislocations nucleate, move, and propagate, eventually recover or pile-up forming sub-grain structures.[45] Several studies have attempted to link the Hall–Petch relationship to the above-mentioned dislocation behavior, and it was suggested that one could develop a Hall–Petch-like law on the effect of the size of dislocations pile-ups or accumulation within grains,[44] which are typical for 316L stainless steel built by L-PBF (cellular network). In that regard, one would expect that the 1 mm samples built with high speed are stronger than those built with standard speed. However, the properties of the latter are relatively similar to the samples built at higher speed. The stronger texture of the standard specimen likely balances the effect of the smaller cell size produced by the high laser scan speed. Moreover, the effect of preferential orientation on the anisotropic behavior of metals has been studied by several research groups and shown to be more predominant in hexagonal systems, like magnesium and titanium, than in cubic ones[46,47] (*e.g.*, "earing" formation of deep drawn cups because of prior in-plane anisotropy introduced by rolling[48]). In general, the strength and plastic deformation of a single grain of specific

Table IV. Average Grain Size Factor Measured Using the EBSD Orientation Maps Along the Building Direction for the Thin Samples Built in Argon, Nitrogen, and Helium with the Standard and the Increased Laser Scanning Speed

Process Gas	3 mm Standard Speed (μm)	1 mm Standard Speed (μm)	1 mm High Speed (μm) (μm)
Argon	23 ± 5	23 ± 6	17 ± 3
Nitrogen	22 ± 3	17 ± 1	15 ± 1
Helium	24 ± 4	23 ± 3	14 ± 4

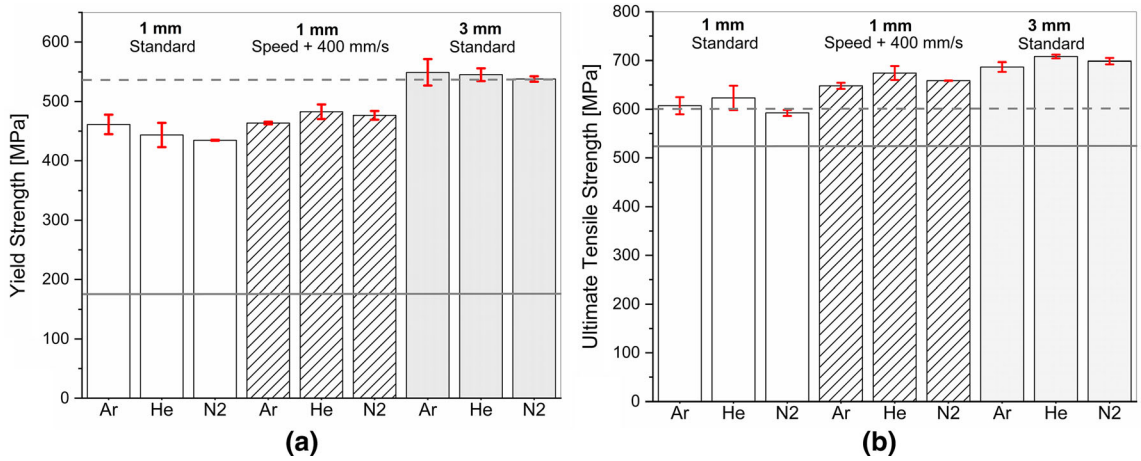

Fig. 6—(*a*) Yield strength and (*b*) ultimate tensile strength of the 1 mm and 3 mm tensile specimens built under argon, helium, and nitrogen, using the standard scanning speed and the increased scanning speed (extra 37 pct). The dashed lines indicate the properties of standard TS bars built using standard process parameters and dimensions according to ASTM E8/E8M-15a. The bold lines correspond to the properties required to fulfill the ASTM 40/A240M-18 (cold formed stainless steel 316L).

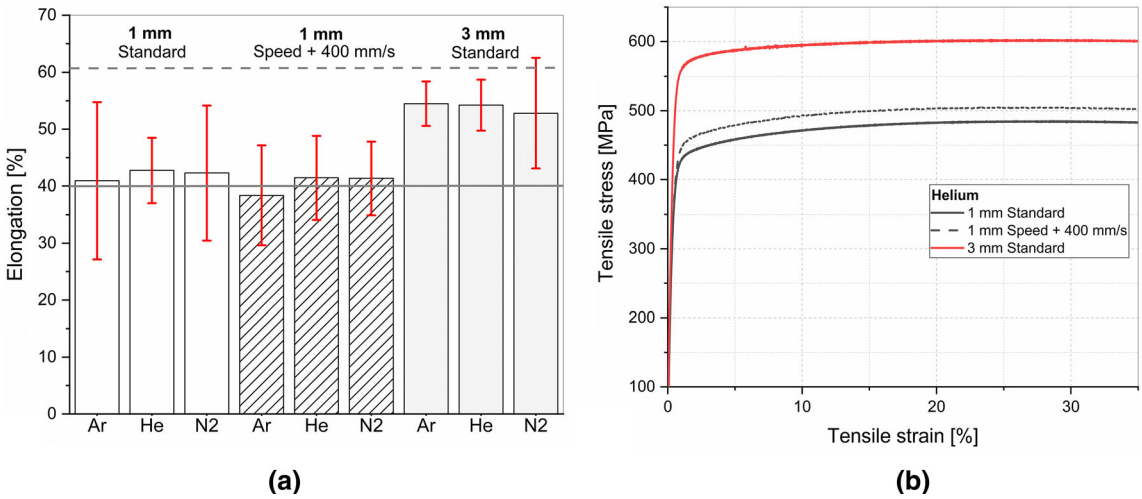

Fig. 7—(*a*) Elongation of the 1 mm and 3 mm tensile specimens built under argon, helium, and nitrogen, using the standard scanning speed and the increased scanning speed (extra 37 pct). The dashed line indicates the properties of samples built using standard process parameters and dimensions according to ASTM E8/E8M-15a. The bold line corresponds to the properties required to fulfill the ASTM 40/A240M-18 (cold formed stainless steel 316L). (*b*) The corresponding stress–strain curves for samples built under helium.

crystallographic orientation are anisotropic. Knowing the tensile loading axis with respect to the orientation of the crystal, one can compute the critical resolved shear stress and Schmid factor to find out which slip systems are preferentially activated. For an fcc crystal, the stiffest orientation is typically ⟨111⟩, and the softest occurs close to the center of the stereographic triangle.[48] For polycrystals, such as the investigated specimens, the properties can be estimated from the average values of the individual crystal orientations weighted to the frequency in which they appear and their sizes. In Figure 4, large and long grains of strong ⟨101⟩ orientation can be identified and are likely to contribute to the strengthening of the material built with

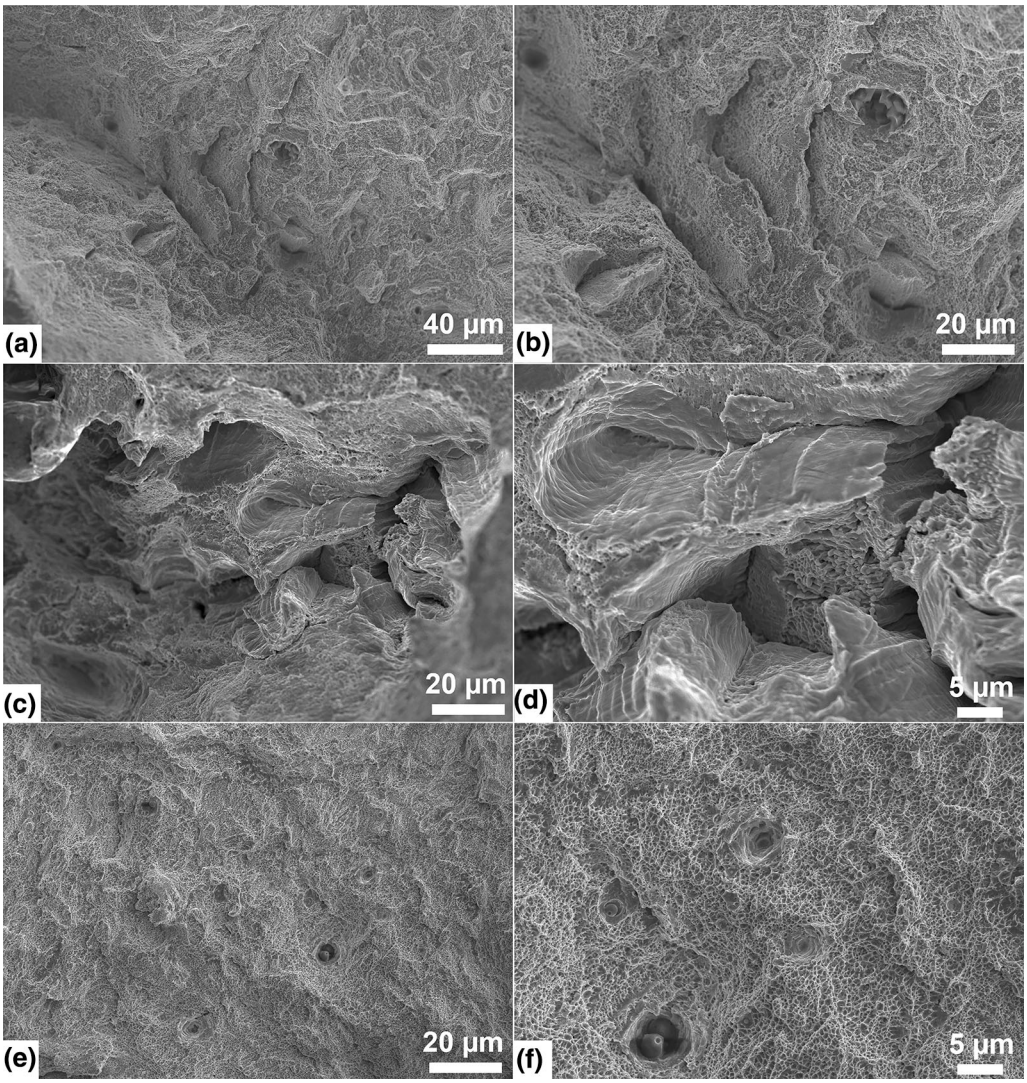

Fig. 8—SEM micrographs of the fracture surface of the 1 mm tensile specimens produced in (*a*), (*b*) argon and (*c*), (*d*) nitrogen and SEM micrographs of the fracture surface of the 3 mm tensile specimens produced in argon (*e*), (*f*).

standard parameters when loaded along the building direction. Furthermore, Sun *et al*.[49] studied the effect of texture specifically on the mechanical response of 316L stainless steel parts built by L-PBF. They produced samples with different textures ($\langle 001 \rangle$ and $\langle 101 \rangle$ along the building direction) by varying the energy input and scanning strategy. Their results highlighted that deformation by twinning is not favorable for the $\langle 001 \rangle$ orientation aligned along the loading direction, while the $\langle 101 \rangle$ orientation enabled the formation of an important number of nano-twins promoting strain hardening and increasing the samples' toughness. Such a texture effect can be expected for the samples built with the standard laser parameters.

Figure 7(b) displays the stress–strain curves recorded during the testing of the thin specimens built in helium. Only the data for samples built in helium are displayed since the curves for the argon and nitrogen samples are comparable. In addition to the apparent difference in strength between the 1 and 3 mm samples, it is clear that they all exhibit a steady work-hardening, as was also shown by Wang *et al*.[29] The authors emphasized the role of the cellular network and its hindering effect on the movement of dislocations. This behavior is apparently maintained regardless of the nature of the process atmosphere. However, further work should be conducted to investigate the effect of the process gas on the residual stresses developed in the built parts as it was shown to possibly be affected by helium additions. Still, as highlighted by Morris Wang *et al*.,[29] residual stresses at the sub-grain level are more critical than residual stresses at the grain level for the mechanical properties.

The possible size and texture effects are valid for all the investigated process atmospheres for thin walls. While the effect of the thickness appears obvious, the change in process gas did not have a similar impact on the material's strength. Still, the material produced in helium with the increased build rate seems characterized by a slightly higher strength for 1 mm samples with YS $= 483 \pm 12$ MPa than for the other two

atmospheres (464 ± 2 MPa for argon and 477 ± 7 MPa for nitrogen). In a similar manner for the UTS, one can note for example that it is 675 ± 14 MPa for helium and 648 ± 6 MPa for argon. This difference could be explained by the finer cell size measured for the helium samples (see Table I). The higher oxygen and nitrogen levels of the helium samples could also contribute to solid solution strengthening (similar to that of nitrogen specimens, see Table I). However, the analysis of the fracture surfaces did not reveal differences in inclusion distribution and sizes between specimens (in terms of oxides since no nitrides were detected). The software JMatPro can be used to calculate the theoretical possible effect of the different O and N contents reported in Table I on the mechanical properties of austenitic 316L stainless steel. Taking an average grain size factor of 23 μm along the building direction for all the 3 mm thick samples, the expected strength difference between the Ar and N_2 (of higher N_2 contents) samples is less than 5 MPa, which is consistent with the uniform results reported in Figure 6. Therefore, solid solution strengthening by nitrogen as an interstitial is minor compared to the cell size network strengthening. These results are similar to those obtained on standard tensile bars.[5] In this previous work, the specimens built under argon exhibited a YS of 566 ± 9 MPa, which compared to the samples built under nitrogen (569 ± 8 MPa) with standard parameters and under standard process atmosphere purities. This similarity between Ar and N_2 processing was connected to a limited nitrogen pick-up under nitrogen atmosphere because of the high cooling rates involved during L-PBF and the too slow kinetics of the reaction. The differences between the reported YS for the standard specimens for the studies performed by Pauzon *et al.*[5] (horizontal specimens XY) and Leicht *et al.*[22] (vertical specimens Z) are likely explained by the anisotropy of 316L stainless steel parts produced by L-PBF.[50]

Helium was successfully implemented as a possible L-PBF process gas without compromising the mechanical performances of the 316L stainless steel parts. The process window should be further extended to higher build rates to further establish the possible benefits of using helium.

IV. CONCLUSION

The present work highlights that the scope of gas supply available for L-PBF of 316L stainless steel can be broadened to cover argon, nitrogen, and helium. Helium presents promising properties with respect to process stability and, therefore, increased process robustness and productivity. The following conclusions can be drawn:

- Helium was successfully implemented as an L-PBF process gas for 316L stainless steel by achieving high density using standard process parameters (> 99.97 pct) and increased build rate parameters (> 99.93 pct), strength (YS = 545 ± 11 MPa for 3 mm sample), and elongation at break (54 ± 4 pct for 3 mm samples), comparable to that obtained with the more traditionally employed argon and nitrogen.
- The samples produced under helium seem to exhibit a finer cellular structure, which can be connected to enhanced cooling rates, explained by the thermal properties of helium and its lower density.
- The EBSD analysis highlighted similar grain structures and preferential orientation among the thin samples built with standard parameters regardless of the process atmosphere. The commonly reported ⟨101⟩ preferential orientation in the building direction for 316L stainless steel parts built by L-PBF was obtained.
- The 3 mm samples exhibit mechanical properties close to the standard dimension according to ASTM E8/E8M-15a and surpass those necessary to fulfill the strength requirements for cold rolled 316L stainless steel (ASTM40/A240M-18). However, thin 1 mm samples exhibit lower mechanical properties with the YS > 430 MPa, UTS > 590 MPa, and E_{AB} > 30 pct. These results were attributed to the surface roughness and the size effect phenomenon.
- The 1 mm samples produced with an enhanced build rate of 37 pct are characterized by a smaller cell size, a weaker texture, and about 30 pct smaller grain size factor along the building direction than the 1 mm samples built with standard laser parameters. Still, the mechanical response of the two types of 1 mm samples are similar. This similarity was attributed to the balanced effect of strengthening by the cellular network and the texture effect.
- A higher oxygen pick-up for the thinner samples was noted and attributed to the higher specific surface area and the connected heat accumulation compared to the 3 mm samples. Still, its effect on the mechanical performance remained minor at the levels observed in this study.

The presented results indicate a high potential for utilizing He as a process gas to widen the process window to higher build rates, even above the 37 pct demonstrated in this study. Further work on argon-helium mixtures could offer a wide range of thermal properties and densities, as well as cost-competitiveness.

ACKNOWLEDGMENTS

Open access funding provided by Chalmers University of Technology. This work was conducted in the framework of the Centre for Additive Manufacturing – Metal (CAM^2) and the AMLight project within the Innovation Program Metallic Materials, both supported by the Swedish Governmental Agency of Innovation Systems (Vinnova).

REFERENCES

1. A. Bin, I. Halimi, and Q. Pham: *Powder Technol.*, 2019, vol. 352, pp. 103–16.
2. W.E. King, A.T. Anderson, R.M. Ferencz, N.E. Hodge, C. Kamath, S.A. Khairallah, and A.M. Rubenchik: *Addit. Manuf. Handb. Prod. Dev. Def. Ind.*, 2017, vol. 041304, pp. 461–506.
3. M. Simonelli, C. Tuck, N.T. Aboulkhair, I. Maskery, I. Ashcroft, R.D. Wildman, and R. Hague: *Metall. Mater. Trans. A*, 2015, vol. 46, pp. 3842–51.
4. E. Hryha, R. Shvab, H. Gruber, A. Leicht, and L. Nyborg: *La Metall. Ital.*, 2018, vol. 3, pp. 34–39.
5. C. Pauzon, E. Hryha, P. Forêt, and L. Nyborg: *Mater. Des.*, 2019, vol. 179, p. 107873.
6. H. Alsalla, L. Hao, and C. Smith: *Mater. Sci. Eng. A*, 2016, vol. 669, pp. 1–6.
7. Y. Liu, J. Zhang, Z. Pang, and W. Wu: *Opt. Lasers Eng.*, 2018, vol. 103, pp. 34–45.
8. F. Calignano, G. Cattano, and D. Manfredi: *J. Mater. Process. Technol.*, 2018, vol. 255, pp. 773–83.
9. H. Yang, J. Yang, W. Huang, Z. Wang, and X. Zeng: *Mater. Des.*, 2018, vol. 156, pp. 407–18.
10. K. Lin, L. Yuan, and D. Gu: *J. Mater. Process. Technol.*, 2019, vol. 267, pp. 34–43.
11. X. Wang, J.A. Muñiz-Lerma, O. Sanchez-Mata, M. Attarian Shandiz, N. Brodusch, R. Gauvin, and M. Brochu: *Scr. Mater*, 2019, vol. 163, pp. 51–56.
12. E. Abele, T. Reiber, M. Hampe, M.C. Bermúdez Agudelo, and F. Menz: *Prog. Addit. Manuf.*, 2019, vol. 4, pp. 451–63.
13. A. Rubenchik, S. Wu, S. Mitchell, I. Golosker, M. LeBlanc, and N. Peterson: *Appl. Opt.*, 2015, vol. 54, p. 7230.
14. A. Leicht, U. Klement, and E. Hryha: *Mater. Charact.*, 2018, vol. 143, pp. 137–43.
15. X. Wang, J.A. Muñiz-Lerma, O. Sánchez-Mata, M. AttariAnShandiz, and M. Brochu: *Mater. Sci. Eng. A*, 2018, vol. 736, pp. 27–40.
16. H.C. Dey, S.K. Albert, A.K. Bhaduri, and U. Kamachi Mudali: *Weld World*, 2013, vol. 57, pp. 903–12.
17. B. Zhang: Université de Belfort-Montbéliard, 2013.
18. X.J. Wang, L.C. Zhang, M.H. Fang, and T.B. Sercombe: *Mater. Sci. Eng. A*, 2014, vol. 597, pp. 370–75.
19. C. Pauzon, P. Forêt, E. Hryha, T. Arunprasad, and L. Nyborg: *J. Mater. Process. Technol.*, 2019, vol. 279, p. 116555.
20. C. Pauzon, P. Forêt, E. Hryha, and T. Arunprasad: in *WorldPM2018*, WorldPM 2018 Bejijng, 2018, pp. 1633–9.
21. S.S. Babu, L. Love, R. Dehoff, W. Peter, T.R. Watkins, and S. Pannala: *MRS Bull.*, 2015, vol. 40, pp. 1154–61.
22. A. Leicht, M. Rashidi, U. Klement, and E. Hryha: *Mater. Charact.*, 2019, vol. 159, p. 110016.
23. M.P. Haines, N.J. Peter, S.S. Babu, and E.A. Jägle: *Addit. Manuf.*, 2020, p. 101178.
24. K. Dietrich, J. Diller, S.D. Go, D. Bauer, and P. Forêt: https://doi.org/10.1016/j.addma.2019.100980.
25. G. Sander, S. Thomas, V. Cruz, M. Jurg, and N. Birbilis: *X. Gao*, 2017, vol. 164, pp. 250–57.
26. J.A. Cherry, H.M. Davies, S. Mehmood, N.P. Lavery, S.G.R. Brown, and J. Sienz: *Int. J. Adv. Manuf. Technol.*, 2014, vol. 76, pp. 869–79.
27. M.L.G. Byrnes, M. Grujicic, and W.S. Owen: *Acta. metall.*, 1987, vol. 35 (7), pp. 1853–62.
28. Y. Zhong, L. Liu, S. Wikman, D. Cui, and Z. Shen: *J. Nucl. Mater.*, 2016, vol. 470, pp. 170–78.
29. Y.M. Wang, T. Voisin, J.T. Mckeown, J. Ye, N.P. Calta, Z. Li, Z. Zeng, Y. Zhang, W. Chen, T.T. Roehling, R.T. Ott, M.K. Santala, P.J. Depond, M.J. Matthews, A.V. Hamza, and T. Zhu: *Nat. Mater.*, 2018, vol. 17, pp. 63–73.
30. A. Leicht, M. Rashidi, U. Klement, and E. Hryha: *Mater. Charact.*, 2020, vol. 159, pp. 1–11.
31. D. Wang, C. Song, Y. Yang, and Y. Bai: *Mater. Des.*, 2016, vol. 100, pp. 291–99.
32. T. DebRoy, H.L. Wei, J.S. Zuback, T. Mukherjee, J.W. Elmer, J.O. Milewski, A.M. Beese, A. Wilson-Heid, A. De, and W. Zhang: *Prog. Mater Sci.*, 2018, vol. 92, pp. 112–24.
33. S. Henry, T. Minghetti, and M. Rappaz: *Acta Mater.*, 1998, vol. 46, pp. 6431–43.
34. S. Suwas, R.K. Ray, and R.K.R. Satyam Suwas: *Crystallographic Texture of Materials*, 2014.
35. P. Krakhmalev, G. Fredriksson, K. Svensson, I. Yadroitsev, I. Yadroitsava, M. Thuvander, and R. Peng: *Metals (Basel)*, 2018, vol. 8, pp. 1–18.
36. O. Andreau, I. Koutiri, P. Peyre, J.D. Penot, N. Saintier, E. Pessard, T. De Terris, C. Dupuy, and T. Baudin: *J. Mater. Process. Technol.*, 2019, vol. 264, pp. 21–31.
37. F. Geiger, K. Kunze, and T. Etter: *Mater. Sci. Eng. A*, 2016, vol. 661, pp. 240–46.
38. Y.J. Yin, J.Q. Sun, J. Guo, X.F. Kan, and D.C. Yang: *Mater. Sci. Eng. A*, 2019, vol. 744, pp. 773–77.
39. L. Liu, Q. Ding, Y. Zhong, J. Zou, J. Wu, Y. Chiu, J. Li, Z. Zhang, Q. Yu, and Z. Shen: *Mater. Today*, 2018, vol. 21, pp. 354–61.
40. M.S. Pham, B. Dovgyy, and P.A. Hooper: *Mater. Sci. Eng., A*, 2017, vol. 704, pp. 102–11.
41. R.W. Armstrong: *J. Mech. Phys. Solids*, 1961, vol. 9, pp. 196–99.
42. Y. Liu, Y. Yang, S. Mai, D. Wang, and C. Song: *Mater. Des.*, 2015, vol. 87, pp. 797–806.
43. R. Casati, J. Lemke, and M. Vedani: *J. Mater. Sci. Technol.*, 2016, vol. 32, pp. 738–44.
44. R. Yuan, I.J. Beyerlein, and C. Zhou: *Sci. Rep.*, 2016, vol. 6, pp. 1–9.
45. P.M. (Peter M. Anderson, J.P. Hirth, and J. Lothe: *Theory of Dislocations*.
46. B. Hutchinson: *Mater. Sci. Technol. (United Kingdom)*, 2015, vol. 31, pp. 1393–401.
47. K. Yvell: *Experimental Studies of Deformation Structures in Stainless Steels Using EBSD*, 2018.
48. M.A. Meyers and K.K. Chawla: *Mechanical Behavior of Materials*, Cambridge University Press, Cambridge, 2009.
49. Z. Sun, X. Tan, S.B. Tor, and C.K. Chua: *NPG Asia Mater.*, 2018, vol. 10, pp. 127–36.
50. EOS: 2014, vol. 49, pp. 1–5.